



**HAL**  
open science

# Local Lubrication Model for Spherical Particles within an Incompressible Navier-Stokes Flow

Baptiste Lambert, Lisl Weynans, Michel Bergmann

► **To cite this version:**

Baptiste Lambert, Lisl Weynans, Michel Bergmann. Local Lubrication Model for Spherical Particles within an Incompressible Navier-Stokes Flow. [Research Report] RR-9093, INRIA Bordeaux, équipe MEMPHIS; Université Bordeaux. 2017, pp.1-28. hal-01585066v1

**HAL Id: hal-01585066**

**<https://inria.hal.science/hal-01585066v1>**

Submitted on 11 Sep 2017 (v1), last revised 20 Mar 2018 (v3)

**HAL** is a multi-disciplinary open access archive for the deposit and dissemination of scientific research documents, whether they are published or not. The documents may come from teaching and research institutions in France or abroad, or from public or private research centers.

L'archive ouverte pluridisciplinaire **HAL**, est destinée au dépôt et à la diffusion de documents scientifiques de niveau recherche, publiés ou non, émanant des établissements d'enseignement et de recherche français ou étrangers, des laboratoires publics ou privés.



# Local Lubrication Model for Spherical Particles within an Incompressible Navier-Stokes Flow

Baptiste Lambert, Lisl Weynans, Michel Bergmann

**RESEARCH  
REPORT**

**N° 9093**

September 2017

Project-Teams Memphis





## Local Lubrication Model for Spherical Particles within an Incompressible Navier-Stokes Flow

Baptiste Lambert<sup>\*†</sup>, Lisl Weynans<sup>†‡</sup>, Michel Bergmann<sup>†‡</sup>

Project-Teams Memphis

Research Report n° 9093 — September 2017 — 28 pages

**Abstract:** The problem of the computation of the short-range hydrodynamic forces and torques acting on immersed particles has been addressed in an incompressible Navier-Stokes flow. These so called lubrication effects are essential to the suspension of the particles and are usually poorly captured by direct numerical simulation of particle laden flow. In this paper, we propose a lubrication model for a coupled volume penalization method and discrete element method solver which estimates the unresolved hydrodynamic forces and torques. Corrections are made locally on the surface of the interacting particles without any assumption on the particle global geometry. Experimental validations have been made with promising results using spherical particles.

**Key-words:** Local Lubrication Correction Model, Particle Laden Flow, Direct Numerical Simulations, Coupled VP-DEM

---

\* baptiste.lambert@inria.fr

† Univ. Bordeaux, IMB, UMR 5251, F-33400 Talence, France

‡ CNRS, IMB, UMR 5251, F-33400 Talence, France

**RESEARCH CENTRE  
BORDEAUX – SUD-OUEST**

200 avenue de la Vieille Tour  
33405 Talence Cedex

## Modèle local de lubrification pour des écoulements Navier-Stokes incompressible de particules sphériques

**Résumé :** Les forces de lubrifications jouent un rôle fondamental dans le phénomène de suspension de particules solides dans un fluide visqueux. Ces forces hydrodynamiques de courte distance d'action sont généralement partiellement capturées par la résolution numérique directe des équations de l'écoulement. L'objectif de cet article est de proposer un modèle pour corriger localement les forces et moments de lubrification. Les corrections sont faites directement sur les éléments de surfaces des particules où les effets de lubrification sont sous-estimés, sans hypothèse sur la géométrie globale des particules. Le modèle proposé a été testé sur deux cas expérimentaux dans le cas de particules sphériques.

**Mots-clés :** Modèle local de lubrification, Ecoulement de particules, Interaction fluide structure

## Contents

<b>1</b>	<b>Introduction</b>	<b>3</b>
<b>2</b>	<b>Theoretical Framework for lubrication model</b>	<b>5</b>
2.1	Squeezing Motion of Rigid Spheres . . . . .	5
2.2	Shearing Motion of Rigid Spheres . . . . .	6
<b>3</b>	<b>Collision Model</b>	<b>8</b>
<b>4</b>	<b>Numerical Model</b>	<b>10</b>
4.1	Discretization of the Governing Equations . . . . .	10
4.2	Dynamics of the Particles . . . . .	12
4.3	Numerical Algorithm . . . . .	14
<b>5</b>	<b>Results</b>	<b>17</b>
5.1	Sphere Falling on a Wall . . . . .	17
5.2	Oblique Impact of a Particle on a Wall . . . . .	22
<b>6</b>	<b>Conclusion and Outlook</b>	<b>25</b>
<b>7</b>	<b>Acknowledgements</b>	<b>25</b>

## 1 Introduction

Suspension of solid particles in a liquid is a type of two-phase flow that appears in various industrial applications as well as natural flow. In the environment, sedimentation in rivers or near-coast has an influence on the flow. By understanding the dynamics of the bed-load transport, the evolution of the river-stream can be forecast to prevent abnormal erosion or obstruction of waterways<sup>[1, 2]</sup>. Macroscopic suspensions are also relevant in several industrial applications such as nuclear waste procession, water treatment, reinforced plastics. For dense mixture as uncured solid rocket fuel or concretes, a high concentration of solid particle is desired without compromising the rheological properties and the flowing behavior of the mixture.

Along the years, several numerical methods have been developed to simulate particle laden flows at different scales. However, due to the importance of the fluid-particle interaction only microscale methods are relevant since they fully resolve the flow around each particle. Because of computational cells larger than the particle size, macroscale methods such as Stokesian Dynamics (SD)<sup>[3, 4]</sup> or Force-Coupling Method (FCM)<sup>[5, 6]</sup>, cannot capture the essential details of the flow. Both methods depend on a truncated multipole expansion of the Stokes equations. Thereby they are usually highly specialized (suited only for specific particle shapes) and are inherently restricted to non inertial flows. From the limitations of macroscale methods, Direct Numerical Simulation (DNS) has emerged as an appealing alternative, reachable thanks to modern improvements of computer performances. By solving the governing equations (Navier-Stokes equations) directly without any further assumptions, DNS enables microscale simulations of arbitrary particle shape at the numerical method accuracy level. DNS method can be divided into two classes of methods. The first class considers boundary-fitted approach<sup>[7, 8]</sup> where the fluid filled the meshed domain. As long as the mesh elements are small enough, this approach enables an accurate computation of the boundary layers and interaction between particles. However, as the particles move, the domain needs to be constantly adapted leading to complex and expansive remeshing issues. The computational cost of the remeshing limits three dimensional simulations

to about a hundred of particles<sup>[8]</sup>. In contrast, the second class of DNS method, considers non-boundary-fitted meshes which are more suited to numerical simulations using a large number of particles. In this approach, the whole domain is discretized on an Eulerian fixed grid where particles are immersed. Several techniques are available to simulate the particulate flow using fictitious domain methods<sup>[9, 10, 11, 12, 13, 14, 15]</sup>, encompassing lattice Boltzmann methods<sup>[16]</sup>, immersed boundary methods (IBM)<sup>[17, 18]</sup> and volume penalization method (VP)<sup>[19]</sup>. In this paper, we used the VP approach coupled with a Discrete Element Method (DEM)<sup>[20]</sup> widely used for granular flow simulation. In this fully coupled method, the particles are tracked using Lagrangian markers. The particle dynamics are solved using the computed hydrodynamic forces and torques.

Although microscale methods are able to capture flow details, they are challenged by some short range effects. As two particles are moving toward each other they start to interact throughout the fluid as the separation distance  $a\epsilon$  (where  $a$  denotes the particle radius) becomes small. This well known lubrication effect is due to the draining of interstitial fluid in the gap between the two interacting particles. The normal and tangential components of the lubrication force diverges as the particles collide ( $\epsilon$  tends to 0) as  $\epsilon^{-1}$  and  $\log(\epsilon)$  respectively. At low Reynolds number values, DNS methods should be able to resolve these lubrication forces if the grid spacing is small enough. Typically, the grid spacing should be at least smaller than  $10^{-3}a$  to capture lubrication effects. The computational costs makes long term simulations of concentrated suspensions prohibitive. Most simulations are performed on meshes with grid spacing of about  $10^{-1}a$ , meaning that the accuracy of the description of the lubrication effects, drops as the particles come in near contact. Therefore a numerical lubrication model is usually introduced to compensate unresolved lubrication forces. The simplest lubrication model consists in adding the theoretical lubrication force known for two spherical particles (normal<sup>[21]</sup> and tangent<sup>[22]</sup> components) to the computed hydrodynamic force<sup>[23]</sup>. This approach considers that lubrication cannot be captured by the flow solver. Indeed, by adding the theoretical lubrication force, the lubrication partially captured by the solver is counted twice. A more accurate approach is suggested in Stokesian Dynamics, where hydrodynamic forces are split into a long- and a short-range actions. The short-range actions are the so-called lubrication. Hence long-range actions are provided by the solver and short-range actions are modeled via the lubrication theory, avoiding an over estimation of the total hydrodynamic forces. However, this decomposition is not easy to adapt to DNS since the long-range hydrodynamic is not explicitly known. A common technique<sup>[24, 25]</sup> is to perform off-line simulations of two isolated particles using a refine mesh without any lubrication model, for different configurations and the normalized separation distance  $\epsilon$ , in order to estimate the unresolved part of the lubrication forces. From these off-line simulations and the lubrication theory, a tabulation of lubrication corrections is created. Hence the lubrication model for on-line simulations estimates the correction to perform from the tabulation. The accuracy of this method depends on the quality of the tabulation and the diversity of the off-line samples used to create it. Aside from the large computational cost for the creation of the tabulation, the method is also limited to spherical particles since the lubrication theory provides solutions only for sphere-sphere and sphere-wall interactions.

In this paper, a lubrication model for incompressible Navier-Stokes flow without tabulation is proposed. The main feature of our model is a local correction of the lubrication effects on the particle surface without any assumption on the particle global geometry. This article is organized as follows. In section 2, we present the theoretical background of our model based on a similar framework than the lubrication theory. Section 3 briefly introduces the soft sphere model developed by Walton *et al.*<sup>[26]</sup> to model particle collisions. Section 4 details the numerical method used to solved the particle laden flow, and the algorithmic procedure. Finally, two experimental cases used to validate our local lubrication correction model are presented in the section 5.

## 2 Theoretical Framework for lubrication model

The local lubrication correction model developed in this paper is based on a theoretical framework used in the classic lubrication theory [21, 22]. Furthermore, the analytic expression of the local lubrication forces and torques have been obtained using methodology as used in the lubrication theory. Therefore, mathematical calculations identical to the lubrication theory are not provided in the paper, and replaced by references to the original authors.

### 2.1 Squeezing Motion of Rigid Spheres

Two smooth particles of radii  $a$  and  $\beta a$  (with  $\beta > 0$ ) immersed in an infinite domain of fluid are considered. One of the particle ( $S_i$ ) is moving at the constant velocity  $\mathbf{U}_i = U_i \mathbf{e}_z$  toward the second stationary particle ( $S_j$ ) (figure 1). The gap between the two particles is denoted  $a\epsilon$  with  $0 < \epsilon \ll 1$ .

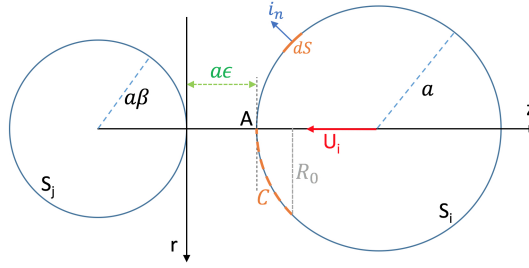


Figure 1: Sketch of the squeeze motion of two particles, with notations.

We consider the flow in the gap in the neighborhood of the contact point  $A$ , such as the Reynolds number in the gap is small ( $Re = \rho U_i a \epsilon / \mu \ll 1$ ). Hence, the flow can be modeled by the Stokes equations (1):

$$\begin{cases} \mu \Delta \mathbf{u} = \nabla p, \\ \nabla \cdot \mathbf{u} = 0, \\ \mathbf{u} \upharpoonright_{\partial S_i} = \mathbf{U} \upharpoonright_{\partial S_i}, \\ \mathbf{u} \upharpoonright_{\partial S_j} = \mathbf{U} \upharpoonright_{\partial S_j}, \\ \lim_{r \rightarrow +\infty} p = 0, \end{cases} \quad (1)$$

where  $\mathbf{u}$  is the velocity field,  $p$  is the pressure field,  $\rho$  is the fluid density and  $\mu$  the fluid dynamic viscosity.

The system (1) is transformed by introducing the Stokes stream-function  $\psi$  in the cylindrical coordinate system  $(r, \theta, z)$  defined such that  $(u_r, u_\theta, u_z) = (\frac{1}{r} \partial_z \psi, 0, -\frac{1}{r} \partial_r \psi)$ . [27, 28, 29]

$$(1) \Leftrightarrow \begin{cases} \Phi^4(\psi) = 0, \\ \psi \upharpoonright_{\partial S_i} = \frac{1}{2} U_i r^2, \\ \psi \upharpoonright_{\partial S_j} = 0, \end{cases} \quad (2)$$

with  $\Phi^2(\cdot) = r \partial_r (\frac{1}{r} \partial_r (\cdot)) + \partial_z^2 (\cdot)$ . The stream-function  $\psi$  solution of (2) can be found near the particle surface  $\partial S_i$  via the Taylor expansion of  $\psi$  as detailed by Jeffrey *et al.* [28]



The lubrication force is due to the hydrodynamic effect of the interaction of the given particle with a nearby obstacle. Thereby, the force is given by the action of the fluid stress on the surface of a particle when this particle and the interacting obstacle are isolated in an unbounded domain (flow field at rest far from the particles). The lubrication force is directly obtained by integration of the fluid stress  $\bar{\bar{\sigma}}$  acting on an element of the surface of the considered particle.

$$\bar{\bar{\sigma}} = -p\bar{\bar{I}} + \mu (\nabla \mathbf{u} + (\nabla \mathbf{u})'). \quad (3)$$

with  $\bar{\bar{I}}$  the identity matrix.

Due to the symmetry of the flow, only the stress induced by a force acting parallel to the axis of revolution ( $Oz$ ) is relevant. Thus the lubrication force on  $S_i$  is:

$$\mathbf{F}_i^{lub} = \int_{\partial S_i} \sigma_{\mathbf{z}} \cdot \mathbf{i}_{\mathbf{n}} dS, \quad (4)$$

with  $\mathbf{i}_{\mathbf{n}}$  the outgoing unit vector of the surface element  $dS$  of the particle  $S_i$  as shown figure 1.

To simplify expressions, the following "stretched" coordinates are introduced:

$$\begin{cases} R &= \frac{r}{a\sqrt{\epsilon}}, \\ Z &= \frac{z}{a\epsilon}, \\ H &= Z_i - Z_j = 1 + \frac{1+\beta}{2\beta}R^2 + O(\epsilon). \end{cases} \quad (5)$$

Via straightforward calculations and simplifications detailed by Happel *et al.*<sup>[30]</sup>, the lubrication force on the particle  $S_i$  is expressed as a function of  $\psi$ , solution of (2), as follows:

$$\mathbf{F}_i^{lub} = \pi\mu \int_C r^3 \partial_n \left( \frac{\Phi^2(\psi)}{r^2} \right) ds \mathbf{e}_{\mathbf{z}}. \quad (6)$$

Where  $ds = \sqrt{\epsilon} (1 + \frac{1}{2}\epsilon R^2) dR + O(\epsilon^{3/2})$  and  $\partial_n = -\epsilon^{-1}\partial_Z + \frac{1}{2}R^2\partial_Z + R\partial_R + O(\epsilon)$  in the "stretched" coordinates<sup>[27, 28, 30]</sup> (5). The "inner" region where the solution  $\psi$  of (2) is defined by  $C = [0, R_0]$  (see figure 1).

Therefore the dominant order (in  $\epsilon$ ) of the lubrication force in the "inner" region is given by:

$$\frac{\mathbf{F}_i^{lub,in}}{\pi\mu a U_i} = -\frac{6R_0^4}{4H_0^2} \frac{1}{\epsilon} \mathbf{e}_{\mathbf{z}} + O(1). \quad (7)$$

To obtain the lubrication force on the whole surface, the lubrication force on the "outer" region needs to be added to the contribution from the "inner" region (7). This can be done by solving (6) with  $\psi$  solution of a Stokes problem in the "outer" region and matching this solution to the solution in the "inner" region<sup>[28]</sup>. Another approach is to match the "inner" solution (7) with a solution on the "outer" region obtained via a detailed numerical simulation<sup>[27]</sup>. At the end, both methods give the dominant order of the total lubrication force as follows:

$$\frac{\mathbf{F}_i^{lub}}{\pi\mu a U_i} = -\frac{6}{\epsilon} \mathbf{e}_{\mathbf{z}} + O(1). \quad (8)$$

## 2.2 Shearing Motion of Rigid Spheres

As for the squeezing motion, two smooth particles of radii  $a$  and  $\beta a$ , with  $\beta > 0$ , are immersed in an infinite domain of fluid. The particle  $S_i$  is now moving near the stationary particle  $S_j$

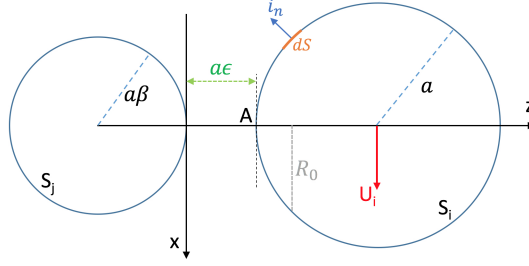


Figure 2: Sketch of the shear motion of two particles, with notations.

at the velocity  $\mathbf{U}_i = U_i \mathbf{e}_x$  (see figure 2). The gap between the two particles is denoted by  $a\epsilon$  ( $0 < \epsilon \ll 1$ ) such as the gap Reynolds number is small ( $Re = \rho U_i a \epsilon / \mu \ll 1$ ).

According to Kim *et al.*<sup>[27]</sup>, symmetries in the flow field in the gap suggest that  $(\mathbf{u}, p)$  can be written in the cylindrical coordinate system  $(\mathbf{i}_r, \mathbf{i}_\theta, \mathbf{i}_z)$  as follows:

$$\begin{cases} u_r = U_i U(r, z) \cos(\theta), \\ u_\theta = U_i V(r, z) \sin(\theta), \\ u_z = U_i W(r, z) \cos(\theta), \\ p = \frac{\mu U_i}{a} P(r, z) \cos(\theta). \end{cases} \quad (9)$$

With  $\theta$  defined such that  $\mathbf{i}_r = \cos(\theta)\mathbf{e}_x + \sin(\theta)\mathbf{e}_y$ , and  $U, V, W$ , and  $P$  are unknown functions such as the velocity and pressure fields are solutions of the Stokes problem (1). Via regular expansion of  $U, V, W$ , and  $P$  and the Taylor expansion of  $\mathbf{u}$  and  $p$  at the particle surface  $\partial S_i$ , the dominant order (in  $\epsilon$ ) of  $(\mathbf{u}, p)$  solution of (1) can be found as detailed by O'Neill *et al.*<sup>[22]</sup>. In particular, the dominant orders of  $U, V$  and  $P$  such as  $(\mathbf{u}, p)$  solution of (1) are:

$$\begin{cases} U_0(R, Z) = -\frac{1}{2} \frac{dP_0}{dR} (Z - Z_j)(Z_i - Z) + \frac{Z - Z_j}{H}, \\ P_0(R) = \frac{6R}{5H^2} \left(1 - \frac{1}{\beta}\right), \\ V_0(R, Z) = -\frac{1}{2} \frac{P_0}{R} (Z - Z_j)(Z_i - Z) - \frac{Z - Z_j}{H}, \end{cases} \quad (10)$$

in the "stretched" coordinates (5).

As for the squeezing motion, the lubrication forces and torque are directly obtained by integration of the fluid stress  $\bar{\sigma}$  (3) over the particle surface  $\partial S_i$ . Due to the symmetry of the flow, only the component of the force according to the  $(Ox)$  is non zero. Hence, the lubrication shear force and torque over an element of surface  $dS$  of  $\partial S_i$ , are given by:

$$\begin{cases} d\mathbf{F}_x = (\bar{\sigma} \cdot \mathbf{i}_n) \cdot \mathbf{e}_x \mathbf{e}_x, \\ d\mathbf{T}_y = (\bar{\sigma} \cdot \mathbf{i}_n) \wedge \mathbf{e}_y. \end{cases} \quad (11)$$

By substitution of  $(\mathbf{u}, p)$ , expressed as (9), solution of the Stokes equation (1), the dominant order (in  $\epsilon$ ) of the lubrication force and torque in the "inner" region are found:

$$\frac{F_x}{a\mu\pi U_i} = \int_0^{R_0} [-P_0 R + \partial_Z V_0 - \partial_Z U_0] R dR + O(\epsilon), \quad (12)$$

$$\frac{T_y}{a^2\mu\pi U_i} = \int_0^{R_0} [\partial_Z U_0 - \partial_Z V_0] R dR + O(\epsilon). \quad (13)$$

To get the lubrication force and torque on the whole surface  $\partial S_i$ , the force and torque acting by the fluid on the "outer" region still need to be calculated and  $R_0$  properly found to connect the two partial contributions<sup>[22]</sup>. However this is not useful for the local lubrication correction model.

### 3 Collision Model

In a Stokes flow, the contact between obstacles is theoretically impossible due to the lubrication singularity. However a collision model needs to be considered for physical and numerical purposes.

From a physical perspective, the lubrication effect alone cannot explain some phenomena such as rebound of particle onto a wall which occurs at the Stokes number above roughly<sup>[23]</sup>  $St_d = \frac{\rho_p d U_c}{9\mu} \approx 10$ , with  $\rho_p$ ,  $d$  and  $U_c$  the particle density, diameter and impact velocity respectively. Collision model is seen here as a "low cost" model to mimic the effect of the particle deformation on its trajectory. Furthermore, real surfaces are never perfectly smooth, meaning that contact can occur at the particle roughness scale or at the lubrication film breakdown scale (when the separation distance is close to fluid particle characteristic size).

From a numerical point of view, a cutoff distance for the lubrication forces is usually introduced to ensure the model stability. This cutoff distance prevents the lubrication force (8) to diverge as the particle collides with an obstacle. A control on the time step in order to avoid contact due to time discretization errors is not an option. Indeed, an adaptive time step would certainly improve the capture of the lubricating effects, but in case of colliding particles at the Stokes number regime  $St_d > 10$ , the time step would keep decreasing asymptotically to zero. Therefore, a lubrication cutoff distance and a collision model need to be introduced for stable and finite time simulations.

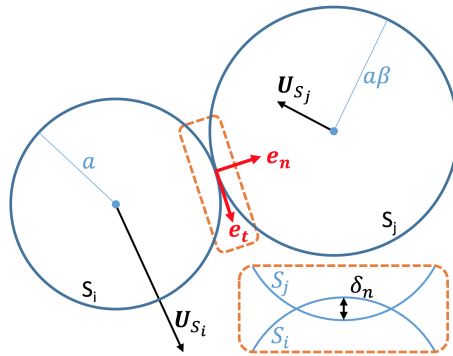


Figure 3: Contact of two particles with notations associated to the soft sphere model.

The collision model chosen here is based on the soft-sphere approach used by Costa *et al.*<sup>[31]</sup>. Deformation of particles during contact is modeled by the overlap between a particle and an obstacle (particle or wall). From the measure of the overlap, normal and tangential contact forces are computed using a mass spring-dashpot system and a Coulomb-type threshold for the tangential component. For a given particle  $S_i$ , collision forces  $\mathbf{F}_i^{col}$  and torque  $\mathbf{T}_i^{col}$  are

decomposed such as:

$$\begin{cases} \mathbf{F}_i^{col} &= \sum_{j \neq i} \mathbf{F}_{S_i S_j} + \mathbf{F}_{Wall}, \\ \mathbf{T}_i^{col} &= \sum_{j \neq i} \mathbf{T}_{S_i S_j} + \mathbf{T}_{Wall}, \end{cases} \quad (14)$$

where  $\mathbf{F}_{S_i S_j}$  is the collision force of the interacting particles  $S_i$  and  $S_j$ ,  $\mathbf{F}_{Wall}$  is the collision force of  $S_i$  with a wall.  $\mathbf{T}_{S_i S_j}$  and  $\mathbf{T}_{Wall}$  are the corresponding collision torques. The force and the torque on  $S_i$  resulting from the particle-particle interactions between  $S_i$  and  $S_j$  are defined as follows using a local system of coordinates  $(\mathbf{e}_n, \mathbf{e}_t)$  (figure 3):

$$\begin{cases} \mathbf{F}_{S_i S_j} &= \mathbf{F}_n + \mathbf{F}_t, \\ \mathbf{T}_{S_i S_j} &= a \mathbf{e}_n \wedge (\mathbf{F}_t), \end{cases} \quad (15)$$

with

$$\begin{cases} \mathbf{F}_n &= -\delta_n k_n - \gamma_n (\mathbf{U}_{i,j} \cdot \mathbf{e}_n) \mathbf{e}_n, \\ \mathbf{F}_t &= \min(\|-\delta_t k_t - \gamma_t (\mathbf{U}_{i,j} \cdot \mathbf{e}_t) \mathbf{e}_t\|, \|\mu_c \mathbf{F}_n\|) \mathbf{e}_t, \end{cases} \quad (16)$$

where  $a$  is the radius of  $S_i$ ,  $\delta_n$  (*resp.*  $\delta_t$ ) is the normal (*resp.* tangential) overlap,  $k_n$  (*resp.*  $k_t$ ) is the normal (*resp.* tangential) stiffness,  $\mu_c$  is the friction coefficient, and  $\gamma_n$  (*resp.*  $\gamma_t$ ) is the normal (*resp.* tangential) damping coefficient of the spring-dashpot model.  $\mathbf{U}_{i,j}$  denotes here the relative velocity of the two particles at the contact point:  $\mathbf{U}_{i,j} = \mathbf{U}_i + a \boldsymbol{\omega}_i \wedge \mathbf{e}_n - (\mathbf{U}_j - a \beta \boldsymbol{\omega}_j \wedge \mathbf{e}_n)$ .

The normal overlap distance  $\delta_n$  is given by

$$\delta_n = \max(0, a(1 + \beta) + \epsilon_{col}(a + \beta a) - \|\mathbf{X}_{S_i} - \mathbf{X}_{S_j}\|) \mathbf{e}_n, \quad (17)$$

with  $\mathbf{e}_n = \frac{\mathbf{X}_{S_i} - \mathbf{X}_{S_j}}{\|\mathbf{X}_{S_i} - \mathbf{X}_{S_j}\|}$  as shown figure 3. The tangential overlap distance  $\delta_t$  is obtained by integrating the relative tangential velocity at the point of contact while the Coulomb's law is verified. Therefore the tangential overlap distance  $\delta_t^{n+1}$  at the time step " $n+1$ " is obtained by

$$\delta_t^{n+1} = \frac{1}{k_t} (-\mu_c \|\mathbf{F}_n\| \mathbf{e}_t - \gamma_t (\mathbf{U}_{i,j} \cdot \mathbf{e}_t) \mathbf{e}_t), \quad (18)$$

when the particle is sliding (*i.e.*  $\|\mathbf{F}_t\| > \mu_c \|\mathbf{F}_n\|$ ) and by

$$\delta_t^{n+1} = \overline{\overline{R}} \cdot \delta_t^n + \int_{t^n}^{t^{n+1}} (\mathbf{U}_{i,j} \cdot \mathbf{e}_t) \mathbf{e}_t dt, \quad (19)$$

when the particle is sticking to the obstacle (*i.e.*  $\|\mathbf{F}_t\| \leq \mu_c \|\mathbf{F}_n\|$ ). The rotation tensor  $\overline{\overline{R}}$  moves  $\delta_t^n$  to the new local coordinate system at the state " $n+1$ ", and  $\mathbf{e}_t = \frac{-\delta_t k_t - \gamma_t (\mathbf{U}_{i,j} - (\mathbf{U}_{i,j} \cdot \mathbf{e}_n) \mathbf{e}_n)}{\|-\delta_t k_t - \gamma_t (\mathbf{U}_{i,j} - (\mathbf{U}_{i,j} \cdot \mathbf{e}_n) \mathbf{e}_n)\|}$ .

The parameters of the spring-dashpot model  $\gamma_n$ ,  $\gamma_t$ ,  $k_n$ , and  $k_t$  are calculated from the coefficient of normal (*resp.* tangential) restitution  $\xi_{max,n}$  (*resp.*  $\xi_{max,t}$ ) of "dry" collision and the contact time  $t_c$ , as follows:

$$\begin{cases} k_n = \frac{m^* (\pi^2 + \ln^2(\xi_{max,n}))}{t_c^2}, & \gamma_n = -\frac{2m^* \ln(\xi_{max,n})}{t_c}, \\ k_t = \frac{m_t^* (\pi^2 + \ln^2(\xi_{max,t}))}{t_c^2}, & \gamma_t = -\frac{2m_t^* \ln(\xi_{max,t})}{t_c}, \end{cases} \quad (20)$$



As reminded by Angot *et al.*<sup>[19]</sup>, solving penalized equation (21) is equivalent to solve the incompressible Navier Stokes in the fluid domain and to enforce a non-slip boundary condition at the boundary  $\Gamma_s$ . This boundary condition is implicitly imposed by the penalty term.

The system (21) is solved in time using a classical projection scheme introduced by Chorin<sup>[33]</sup> and Temam<sup>[34]</sup>. Therefore (21) is "uncoupled" by introducing the virtual pressure and velocity field  $(q, \mathbf{u}^*)$  as follows (22):

$$\left\{ \begin{array}{l} \frac{\mathbf{u}^* - \mathbf{u}^n}{\Delta t} + [(\mathbf{u}\nabla)\mathbf{u}]^{n+1/2} = \nu\Delta\mathbf{u}^{n+1/2} - \frac{1}{\rho}\nabla q \\ \frac{\tilde{\mathbf{u}} - \mathbf{u}^*}{\Delta t} = -\frac{1}{\rho}\nabla p^{n+1} + \frac{1}{\rho}\nabla q, \\ \frac{\mathbf{u}^{n+1} - \tilde{\mathbf{u}}}{\Delta t} = \chi\lambda(\mathbf{u}_\tau - \mathbf{u}^{n+1}). \end{array} \right. \quad (22)$$

Discretizations in space are made using a second order scheme and a third order upwind scheme for the convective term.

The idea is to solve the system (22) in four steps:

1. *Prediction:*

The virtual velocity field  $\mathbf{u}^*$  is obtained by the first equation of (22):

$$\mathbf{u}^* = \mathbf{u}^n - \Delta t \left( [(\mathbf{u}\nabla)\mathbf{u}]^n - \nu\Delta\mathbf{u}^n - \frac{1}{\rho}\nabla q \right). \quad (23)$$

The gradient of the virtual pressure  $\nabla q$  can be set to arbitrary values. However assuming  $q = p^n$  improves the convergence of the projection step.

2. *Projection:*

At the end of projection step,  $\mathbf{u}^*$  is *a priori* not divergence free. The projection step aims to find the pressure field  $p^{n+1}$  such that  $\nabla \cdot \tilde{\mathbf{u}} = 0$ . By applying the divergence operator to the second equation of (22), and enforcing that  $\nabla \cdot \tilde{\mathbf{u}} = 0$ , the following equation is found:

$$\nabla \cdot \mathbf{u}^* = \frac{\Delta t}{\rho} \nabla^2 (p^{n+1} - q). \quad (24)$$

And in particular, the following linear problem is solved:

$$\nabla \cdot \mathbf{u}^* = \Delta t \nabla^2 \Phi. \quad (25)$$

with  $\Phi = \frac{p^{n+1} - q}{\rho}$  the unknown.

3. *Correction:*

From the solution  $\Phi$  of the Poisson equation (25) the pressure and velocity fields  $(p^{n+1}, \tilde{\mathbf{u}})$  are given by:

$$\begin{array}{l} p^{n+1} = \rho\Phi + p^n, \\ \tilde{\mathbf{u}} = \mathbf{u}^* - \Delta t \nabla \Phi, \end{array} \quad (26)$$

with  $\tilde{\mathbf{u}}$  is divergence free.

#### 4. Penalization:

Finally, the solid velocities of the particles  $\mathbf{u}_\tau$  are penalized (third equation of (22)) in order to obtain the velocity field  $\mathbf{u}^{n+1}$ :

$$\mathbf{u}^{n+1} = \frac{\tilde{\mathbf{u}} + \chi\lambda\Delta t\mathbf{u}_\tau}{1 + \chi\lambda\Delta t}. \quad (27)$$

## 4.2 Dynamics of the Particles

The dynamics of each rigid particle is obtained, as for the Stokesian dynamics, by the following equations:

$$m_i \frac{d\mathbf{U}_i}{dt} = \mathbf{F}_i^{hyd} + \mathbf{F}_i^{coll} + \mathbf{F}_i^{ext} + \mathbf{F}_i^{lub}, \quad (28)$$

$$\bar{I}_i \frac{d\bar{\boldsymbol{\Omega}}_i}{dt} = \mathbf{T}_i^{hyd} + \mathbf{T}_i^{coll} + \mathbf{T}_i^{lub}, \quad (29)$$

for a given particle  $P_i$  of mass  $m_i$ , inertia matrix  $\bar{I}_i$ , linear velocity  $\mathbf{U}_i$  of the mass center and rotational velocity  $\bar{\boldsymbol{\Omega}}_i$ . Fluid action on the particle  $P_i$  is split into two contributions: the hydrodynamic force  $\mathbf{F}_i^{hyd}$  and torque  $\mathbf{T}_i^{hyd}$  which are obtained from the simulated flow around  $P_i$ , and the lubrication force  $\mathbf{F}_i^{lub}$  and torque  $\mathbf{T}_i^{lub}$  given by the lubrication model. The force  $\mathbf{F}_i^{coll}$  and torque  $\mathbf{T}_i^{coll}$  represent the effects of solid contacts of  $P_i$  with obstacles.  $\mathbf{F}_i^{ext}$  is a non-hydrodynamic force like gravity (which is the only external force which we considered).

In our framework  $\mathbf{F}_i^{coll}$  and  $\mathbf{T}_i^{coll}$  are given by the collision model described in section 3 ( $\mathbf{F}_i^{coll} \equiv \mathbf{F}_{S_i}^{col}$  and  $\mathbf{T}_i^{coll} \equiv \mathbf{T}_{S_i}^{col}$ ).

The hydrodynamic force  $\mathbf{F}_i^{hyd}$  is computed by numerical integration of the fluid stress on the particle surface:

$$\mathbf{F}_i^{hyd} = \int_{\partial P_i} \mathbf{d}\mathbf{f}^h ds \approx \sum_{k \in \partial P_i} \mathbf{d}\mathbf{f}_k^h ds_k, \quad (30)$$

with  $\mathbf{d}\mathbf{f}_k^h$  the hydrodynamic force exerted by the fluid on the center of the  $k$ -th surface element  $P_i^k$  of  $P_i$  (of surface  $ds_k$ ). The expression of  $\mathbf{d}\mathbf{f}_k^h$  changes depending if local lubrication corrections are needed or not. In other words, if the flow is fully resolved ( $\epsilon > \epsilon_{lub}$ , see figure 5),  $\mathbf{d}\mathbf{f}_k^h$  is directly computed from the simulation. Otherwise ( $\epsilon \leq \epsilon_{lub}$ ),  $\mathbf{d}\mathbf{f}_k^h$  is given by the lubrication model and will be detailed later.

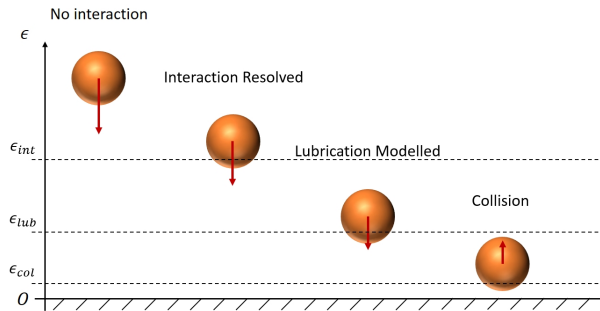


Figure 5: Sketch of the motion of a particle to a wall. The vertical axis shows the different characteristic distances to the wall where lubrication is fully resolved ( $\epsilon_{lub}\epsilon \leq \epsilon_{int}$ ), modeled ( $\epsilon \leq \epsilon_{lub}$ ) and completed by a collision model ( $\epsilon \leq \epsilon_{col}$ ).

When  $\epsilon \leq \epsilon_{lub}$ , the flow in the gap between the two particles in interaction is assumed in the Stokes regime. This hypothesis allows us to split the flow between a regular and a singular field, using the linearity of Stokes flows (equation (31)).

$$\begin{cases} \mathbf{u} = \mathbf{u}^{reg} + \mathbf{u}^{sing}, \\ p = p^{reg} + p^{sing}. \end{cases} \quad (31)$$

The regular field ( $p^{reg}, \mathbf{u}^{reg}$ ) corresponds to the fluid flow unperturbed by the presence of particles. For instance, in the two cases discussed in section 2, both velocity and pressure of the regular field are equal to zero since the two particles are isolated in a fluid initially at rest.

The singular field ( $p^{sing}, \mathbf{u}^{sing}$ ) is created by interacting particles. The action of the singular field of the particles is approximated by the first order (in  $\epsilon$ ) of the force and torque asymptotic expressions given by the lubrication theory. Local lubrication force and torque acting on the particle  $P_i$  interacting with the obstacle  $P_j$  are given respectively by  $\mathbf{df}_{i,j}^{lub}$  and  $\mathbf{dT}_{i,j}^{lub}$  (32):

$$\begin{cases} \mathbf{df}_{i,j}^{lub} &= \mathbf{df}_{i,j}^{lub,sq} + \mathbf{df}_{i,j}^{lub,sh}, \\ \mathbf{dT}_{i,j}^{lub} &= \mathbf{dT}_{i,j}^{lub,sh}, \\ \mathbf{df}_{i,j}^{lub,sq} &= -\pi\mu a U_{i,j}^{sq} \frac{6R_0^4}{4H_0^2} \frac{1}{\max(\epsilon_{col}, \epsilon)} \mathbf{e}_n, \\ \mathbf{df}_{i,j}^{lub,sh} &= \int_0^{R_0} [-P_0 R + \partial_Z V_0 - \partial_Z U_0] R dR \mathbf{e}_t, \\ \mathbf{dT}_{i,j}^{lub,sh} &= \int_0^{R_0} [\partial_Z U_0 - \partial_Z V_0] R dR \mathbf{e}_n \wedge \mathbf{e}_t, \\ U_{i,j}^{sq} &= U_j^{sq} - U_i^{sq}, \\ U_{i,j}^{sh} &= U_j^{sh} - U_i^{sh} + (\omega_j \beta - \omega_i) a, \end{cases} \quad (32)$$

with  $H_0 = 1 + \frac{1}{2}a\alpha R_0^2$ ,  $\alpha = \frac{\beta+1}{a\beta}$ , and  $R_0 = \frac{1}{\sqrt{\epsilon}} \sqrt{1 - (1 + \epsilon - \epsilon_{lub})^2}$  (see figure 7). The local forces  $\mathbf{df}_{i,j}^{lub,sq}$  and  $\mathbf{df}_{i,j}^{lub,sh}$  are respectively induced by the squeezing and shearing relative motion of the particles ((7) and (12)). The torque induced by  $\mathbf{df}_{i,j}^{lub,sh}$  is  $\mathbf{dT}_{i,j}^{lub,sh}$ . The analytic expressions of  $\mathbf{df}_{i,j}^{lub,sh}$  and  $\mathbf{dT}_{i,j}^{lub,sh}$  are not as simple as the expression of  $\mathbf{df}_{i,j}^{lub,sq}$ . Therefore we choose to compute the shearing components by numerical integration (see section 4.3). Furthermore, numerical integration will be necessary if we want to add lower orders of the lubrication forces and torque. The projected relative velocity of the two particles on respectively the direction  $\mathbf{e}_n$  and  $\mathbf{e}_t$  are respectively  $U_{i,j}^{sq}$  and  $U_{i,j}^{sh}$  (see figure 6).

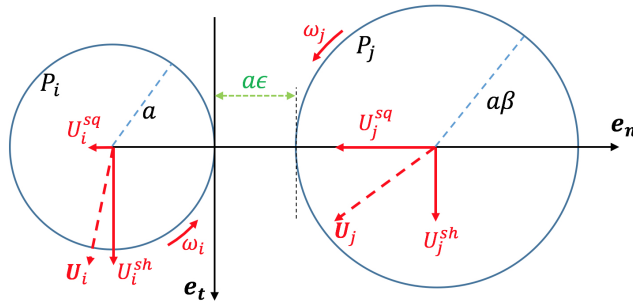


Figure 6: Sketch of the two interacting particles with the notations used for evaluation of  $\mathbf{df}_k^{lub}(j)$ .



Hence the lubrication force  $\mathbf{F}_i^{lub}$  and torque  $\mathbf{T}_i^{lub}$  acting on  $P_i$  and  $\mathbf{df}_k^h$  are given by:

$$\begin{aligned}\mathbf{F}_i^{lub} &= \sum_{j \in \llbracket 1, N \rrbracket \setminus \{i\}} \mathbf{df}_{i,j}^{lub}, \\ \mathbf{T}_i^{lub} &= \sum_{j \in \llbracket 1, N \rrbracket \setminus \{i\}} \mathbf{dT}_{i,j}^{lub},\end{aligned}\tag{33}$$

$$\mathbf{df}_k^h = \begin{cases} (\overline{\overline{\sigma}} \cdot \mathbf{i}_n) & \text{if } \mathbf{L}(P_i^k) = \emptyset, \\ (\overline{\overline{\sigma}}_{reg} \cdot \mathbf{i}_n) & \text{otherwise,} \end{cases}\tag{34}$$

where the stress tensor of the regular field on the particle is noted  $\overline{\overline{\sigma}}_{reg}$ . The set of particle  $P_j$ ,  $j \neq i$  such that the distance of the surface of  $P_j$  and the center of the surface element  $P_i^k$  is lower than  $a\epsilon_{lub}$  is denoted by  $\mathbf{L}(P_i^k)$ . The lubrication model limit  $a\epsilon_{lub}$  is defined as the narrowest gap width between the center of the  $P_i^k$  and a potential nearby obstacle for the solver to fully resolved hydrodynamic interactions. Typically,  $a\epsilon_{lub} \sim 2 - 3$  grid cells (see figure 7).

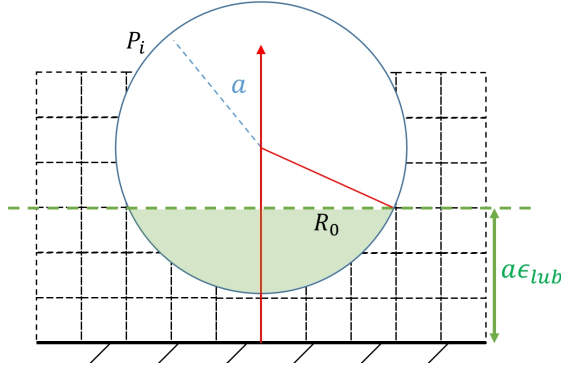


Figure 7: Sketch of the lubrication (in green) where local corrections are performed.

### 4.3 Numerical Algorithm

The full resolution of the system from the current state  $n$  to the state  $n + 1$ , is obtained via the following steps (figure 8):

1. *Estimation of the time step:*

The time step  $\Delta t$  is estimated from the velocities such as the Courant - Friedrichs - Lewy condition is ensured:  $\Delta t = \beta \frac{\Delta x}{V_{max}}$  where  $\beta \leq 1$  is chosen arbitrary,  $\Delta x$  the characteristic length of the grid cells and  $V_{max}$  the maximum of the velocity absolute value computed on the grid cells.

When particles are in near contact, the time step  $\Delta t$  has to satisfy the stability condition of the collision model. Therefore, when lubrication corrections are active (i.e. collision might occur)  $\Delta t$  is chosen such that  $t_c = N_t \Delta t$  (with  $t_c$  the contact time) and  $\Delta t \leq \beta \frac{\Delta x}{V_{max}}$ , with  $N_t > 0$  integer ( $N_t \geq 8$ , in this paper).

2. *Prediction of the virtual velocity field:*

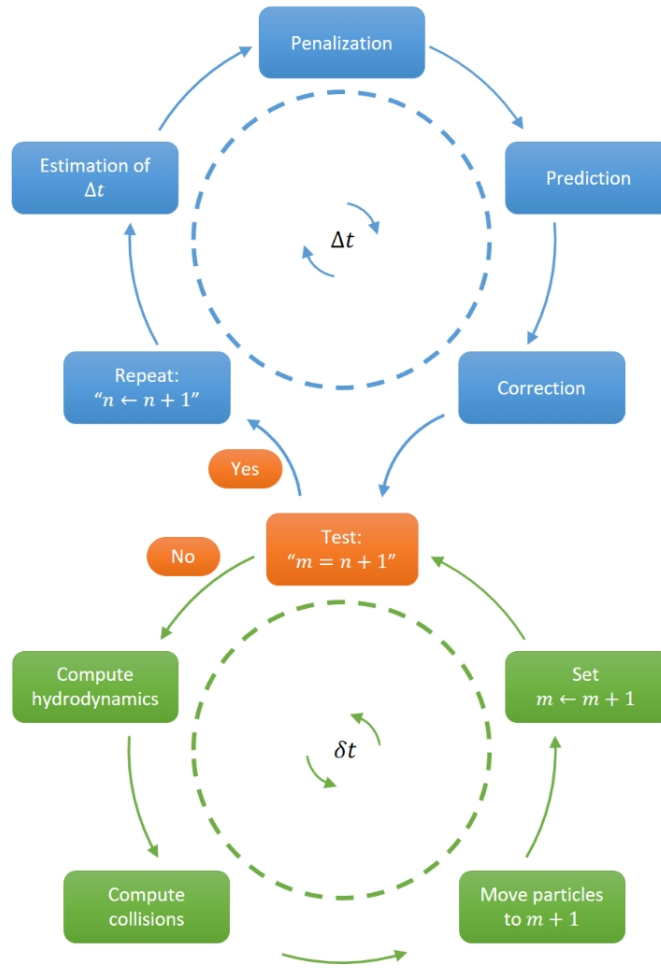


Figure 8: Sketch description of the numerical algorithm used to compute the state  $n + 1$  of the whole system from its state  $n$ . The algorithm starts at the estimation of the time step  $\Delta t$  which is the time elapse between the system state  $n$  and  $n + 1$ . The particle dynamic is solved in  $n_t$  sub-time steps  $\delta t = \frac{\Delta t}{n_t}$ .  $m$  denotes the current sub-state of the system between the state  $n$  and  $n + 1$  while the particle dynamic is computed (NB: after the step "correction", the state  $m$  is equivalent to the state  $n$ )

This is the first step of the projection method where (23) is solved. We have chosen an incremental method meaning that  $q$  is approximated in (23) by  $p^n$ . Via the second order Adams-Bashforth scheme, the convective term becomes:

$$[(\mathbf{u}\nabla)\mathbf{u}]^{n+1/2} \approx \frac{3}{2} [\mathbf{u}\cdot\nabla\mathbf{u}]^n - \frac{1}{2} [\mathbf{u}\cdot\nabla\mathbf{u}]^{n-1}. \quad (35)$$

Then spacial discretization of both terms are obtained by Mittal scheme [35]. The viscous term  $\Delta\mathbf{u}^{n+1/2}$  is approximated using the Crank-Nicolson method

### 3. Correction of the velocity and pressure field:

The velocity field  $\mathbf{u}^*$  is non necessarily divergence free. It is necessary to project it into a divergence free space. The resulting Poisson (25) is solved using the Generalized Minimal Residual method (GMRES) developed by Saad *et al.*<sup>[36]</sup>. At low Reynolds number the iterative method can become costly. Hence preconditioners are used to reduce the number of iteration needed to ensure a divergence free velocity field.

At the end of this step the pressure and velocity field are known at the state  $n + 1$ .

#### 4. Forces & Particle advection:

The particle motions are given by the equations (28) and (29). A smaller time step than  $\Delta t$  is used due to the difference of time scale of the acting forces. Indeed, the time scales of short-range interactions (lubrication and mechanical collision) are at least two orders of magnitude smaller than the fluid time step  $\Delta t$ . Therefore a sub-time step  $\delta t$  is introduced such as  $\delta t = \frac{\Delta t}{n_t}$ , with  $n_t$  arbitrary chosen large. Numerical simulations have shown that changing  $n_t$  between  $10^2$  and  $10^3$  does not affect significantly the results.

Since the motion of the particle occurs at time step smaller than  $\Delta t$ , it is not necessary to re-compute each element of force  $\mathbf{df}_k^h$  (34) of the hydrodynamic force  $\mathbf{F}_i^{hyd}$  (30) at each sub-time step  $\delta t$ . In order to reduce the computation cost, each  $\mathbf{df}_k^h$  is computed once by time step  $\Delta t$  using the pressure and velocity field at the state  $n + 1$  of the fluid. They are then assumed constant for each sub-time step  $\delta t$ . Hence particle dynamics is solved at each sub-time step  $\delta t$  with updated short-range interactions and "frozen" hydrodynamics.

Let us denote by  $m$  the "sub-state" of the system at the time  $t = t_n + m\delta t$  with  $t_n$  the time at the state  $n$  of the system. The mass center velocity and the angular velocity of each particle are given at the state  $m$  by:

$$\begin{aligned} \mathbf{U}_i^{m+1} &= \mathbf{U}_i^m + \frac{\delta t}{m_i} \left[ \mathbf{F}_i^{hyd} \right]^{n+1} \\ &\quad + \frac{\delta t}{m_i} \left[ \mathbf{F}_i^{coll} + \mathbf{F}_i^{ext} + \mathbf{F}_i^{lub} \right]^m. \end{aligned} \quad (36)$$

$$\begin{aligned} \boldsymbol{\Omega}_i^{m+1} &= \boldsymbol{\Omega}_i^m + \delta t \left( \bar{I}_i \right)^{-1} \\ &\quad \left( \left[ \mathbf{T}_i^{hyd} \right]^{n+1} + \left[ \mathbf{T}_i^{coll} + \mathbf{T}_i^{lub} \right]^m \right). \end{aligned} \quad (37)$$

The hydrodynamic effects  $\left[ \mathbf{F}_i^{hyd} \right]^{n+1}$  and  $\left[ \mathbf{T}_i^{hyd} \right]^{n+1}$  are computed using (30) and (34). Each element of force  $\mathbf{df}_k^h$  is obtained by linear interpolation of  $(p^{n+1}, \tilde{\mathbf{u}})$  at the centers of all particle mesh elements in order to get the local fluid stress  $(\bar{\boldsymbol{\sigma}} \cdot \mathbf{i}_n)$ .

Lubrication effects are obtained at each sub-time step via (32). The numerical interpolation method chosen is the composite Simpson's rule at  $n_{lub}$  sub-sets. In other words, the lubrication region  $[0, R_0]$  at the sub-state  $m$  of the particle  $P_i$  interacting with another particle  $P_j$ , is divided into  $n_{lub}$  regular sets. The sum of the integration on each sub-sets by the Simpson's rule (38) gives the total lubrication effect resulting of this specific interaction between  $P_i$  and  $P_j$ .

$$\int_a^b \phi(x) dx \approx \frac{b-a}{6} \left( \phi(a) + 4\phi\left(\frac{a+b}{2}\right) + \phi(b) \right). \quad (38)$$

In details,  $\mathbf{df}_{i,j}^{lub,sh}$  and  $\mathbf{dT}_{i,j}^{lub,sh}$  are given by:

$$\begin{aligned}\mathbf{df}_{i,j}^{lub,sh} &= \sum_{k=1}^{n_{lub}} \int_{\mathbf{R}_k} [-P_0 R + \partial_Z V_0 - \partial_Z U_0] R dR \mathbf{e}_t, \\ \mathbf{dT}_{i,j}^{lub,sh} &= \sum_{k=1}^{n_{lub}} \int_{\mathbf{R}_k} [\partial_Z U_0 - \partial_Z V_0] R dR \mathbf{e}_n \wedge \mathbf{e}_t.\end{aligned}\tag{39}$$

Where  $\mathbf{R}_k = \left[ \frac{k-1}{n_{lub}} R_0, \frac{k}{n_{lub}} R_0 \right]$  and  $R_0 = \frac{1}{\sqrt{\epsilon}} \sqrt{1 - (1 + \epsilon - \epsilon_{lub})^2}$  as defined in section 4.2. Each integral  $\int_{\mathbf{R}_k} \cdot dR$  is then approximated by the Simpson's rule (38).

Mechanical contacts are evaluated at each sub-state  $m$  as described in section 3.

When all forces and torques are known at the sub-state  $m$ , particles are moved to their sub-state  $m+1$  by using (36) and (37). This process is repeated  $n_t$  times, until the system reaches its state  $n+1$ .

#### 5. Penalization of the solid grid cells:

The penalty term is then applied on solid grid cells using (27), with the coefficient of penalization  $\lambda = 10^8$ . To improve the description of the fluid-particle interactions, we used a second order penalty method<sup>[37]</sup>.

#### 6. Repeat Set $n$ to $n+1$ and go to step 1.

## 5 Results

### 5.1 Sphere Falling on a Wall

A single particle is immersed in a domain  $[4d, 4d, 4d]$ , with  $d = 2a$  the particle diameter, uniformly meshed with cubic elements of size  $\Delta x = \Delta y = \Delta z = hd$ . Periodic boundary conditions are considered on the lateral faces of the domain. A no-slip condition is imposed at the top and bottom walls ( $y$  constant). Simulations have been performed on a  $[8d, 8d, 8d]$  domain and have given identical solutions than on the smaller domain. The fluid is initially at rest and the particle is dropped without initial velocity such that the gap size from the bottom wall is given by  $a\epsilon_{init}$  as shown figure 9. The gravity field  $g$  acts on the  $y$ -direction.

In order to have an experimental reference for comparison, we choose the same configuration as one of the two cases from Harada *et al.*<sup>[38]</sup>. Particle and fluid properties are presented in table 1.

Under these configurations (table 1), fluid characteristic Reynolds and Stokes numbers are as follows:

$$\begin{cases} Re_d &= \frac{\rho U_T d}{\mu} \approx 25.7, \\ St_d &= \frac{\rho_p U_T d}{9\mu} \approx 3.27. \end{cases}\tag{40}$$

Figure 10 compares the particle velocity  $U$  simulated using the local lubrication correction model (LLCM) to experimental measurements made by Harada *et al.*<sup>[38]</sup>. Numerical simulations were performed on cartesian mesh with a grid spacing  $h = 1/40$  and using 3200 elements for

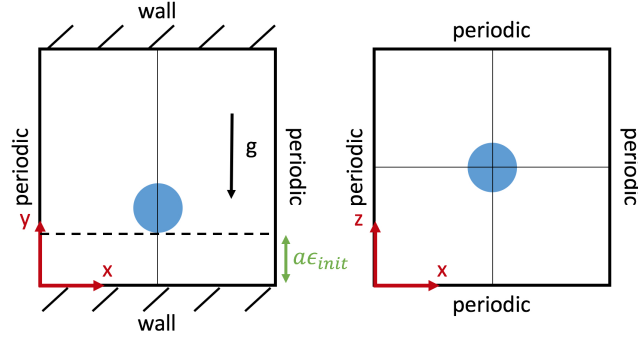


Figure 9: Sketch of two cross sections of the domain with its configuration and initial location of the particle.

Fluid density	$\rho$	985	$kg.m^{-3}$
Fluid dynamic viscosity	$\mu$	0.142	$Pa.s$
Particle density	$\rho_p$	1127	$kg.m^{-3}$
Particle Diameter	$d$	0.0254	$m$
Normal restitution	$\xi_{max}$	0.97	
Contact time	$t_c$	$7.98.10^{-5}$	$s$
Friction coefficient	$\mu_c$	0.25	
Particle roughness	$a\epsilon_{col}$	$2.10^{-4}d$	$m$
Gravity field	$g$	9.781	$N.kg^{-1}$
Terminal Velocity	$U_t$	0.146	$m.s^{-1}$
Initial position	$\epsilon_{init}$	0.4181	

Table 1: Simulation configurations.

the particle surface mesh. Local lubrication correction is performed on particle mesh elements closer than  $2\Delta y$  to the wall. Numerical experiments have shown that the number of particle mesh elements (starting from about a thousand elements) has a limited impact on the solutions. Therefore all the following simulations have been performed using 3200 elements for the particle mesh.

The basic lubrication correction model (BLCM) directly add the results of the lubrication theory as a correction for the lubrication forces and torques. For this approach the same solver than for LLCM can be used by modifying the local hydrodynamic and lubrication forces as follows:

$$\begin{cases} \mathbf{df}_{i,j}^{lub} &= 6\pi\mu a U_{i,j}^{sq} \frac{\mathbf{e}_n}{\max(\epsilon_{col}, \epsilon)}, \\ \mathbf{df}_k^h &= (\bar{\sigma} \cdot \mathbf{i}_n). \end{cases} \quad (41)$$

The BLCM is generally used for a higher Stokes number<sup>[23]</sup> where inertia effects are not negligible. The significant difference between BLCM velocity and experimental measurement shown on figure 10 can be explained by the overestimation of the hydrodynamic force. Indeed, as discussed at the end of the section 2.1, the hydrodynamic force is taken into account twice in the outer region. In addition, in the "inner" region the solver still partially resolve the lubrication force and adds this contribution to the particle total force.

With the local lubrication correction model, the unresolved hydrodynamic force on each

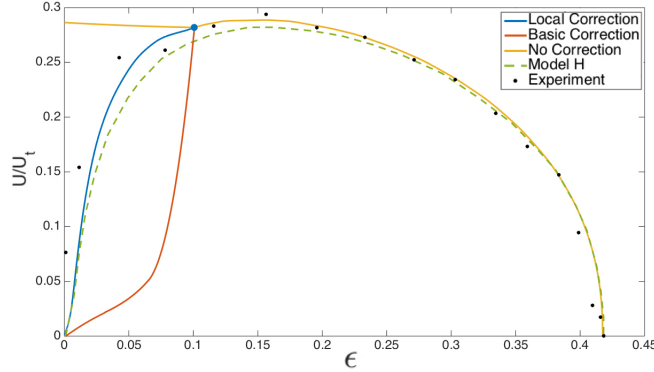


Figure 10: The vertical velocity of the particle in function of the gap non-dimensional size. Simulations using local and basic lubrication correction are compared to Harada<sup>[38]</sup> experimental measurements and the model H.

surface element of the particle within the lubrication area is substituted by the dominant order of the lubrication force for the whole lubrication area only. Therefore, the total hydrodynamic force is better assessed and particle velocity is closer to experimental data (Pearson's correlation coefficient equals to 0.9635,  $L^2|_{local}^{exp} = 0.0165 \text{ m.s}^{-1}$ ,  $L^\infty|_{local}^{exp} = 0.0844 \text{ m.s}^{-1}$ ). The better agreement with measurements comes with a computation cost around 10% higher than BLCM.

We define the relative errors  $L^2|_{\psi}^{\phi}$  and  $L^\infty|_{\psi}^{\phi}$  as the relative errors  $L^2$  and  $L^\infty$  of the solution  $\psi$  compared to the solution  $\phi$ :

$$\begin{aligned} L^2|_{\psi}^{\phi} &= \sqrt{\frac{1}{n} \sum_{i=1}^n (\phi_i - \psi_i)^2}, \\ L^\infty|_{\psi}^{\phi} &= \max_i (|\phi_i - \psi_i|). \end{aligned} \quad (42)$$

Due to the lack of experimental measurements of the total hydrodynamic forces for a falling particle, simulated total hydrodynamic forces are compared to an analytic model ("model H") introduced by Harada *et al.*<sup>[38]</sup>. The model H is based on the Stokesian dynamic, where hydrodynamic forces  $\mathbf{F}_i^{ModelH} = \mathbf{F}_i^{hyd} + \mathbf{F}_i^{lub}$  on the particle are modeled by the dominant order of the lubrication force  $\mathbf{f}_l$ , the added-mass force  $\mathbf{f}_a$  and the history Basset force  $\mathbf{f}_{Ba}$ .

The dominant order of the lubrication force is obtained by integration of the interstitial pressure between the particle and the wall<sup>[39]</sup>:

$$\mathbf{f}_l = 6\pi\mu a \frac{\mathbf{U}_i^{sq}}{\epsilon}. \quad (43)$$

This is the force used as lubrication correction in the BLCM.

As the motion of the particle is unsteady, the added mass force changes near the wall as follows<sup>[40]</sup>:

$$\begin{cases} \mathbf{f}_a &= m' \frac{d\mathbf{U}_i}{dt} + \frac{1}{2} \frac{dm'}{dt} \mathbf{U}_i, \\ m' &= \frac{2}{3} \pi \rho a^3 \left( 1 + \sum_{i=0}^{\infty} \frac{3a^{3(i+1)}}{f_0 f_1 \dots f_i} \right), \end{cases} \quad (44)$$

where  $f_i$  is recursively defined such that  $f_0 = 2a(\epsilon + 1)$  and  $f_i = f_0 - a^2/f_{i-1}$ .

The Basset history force for a spherical particle is given by:

$$\mathbf{f}_{Ba} = 6a^2 \sqrt{\pi\rho\mu} \int_{-\infty}^t \frac{d\mathbf{U}_i}{dt'} \frac{dt'}{\sqrt{t-t'}}. \quad (45)$$

Hence the hydrodynamic force of the model H  $\mathbf{F}_i^{ModelH}$  is obtained by the sum of (43),(44) and (45).

Numerical simulations have shown than simulated velocities using the LLCM tend to experimental measurements as  $h$  decreased. Table of convergence 2 shows that the order of the numerical method used is closed to a second order in  $L^2$  and  $L^\infty$  on velocities (for  $h > 1/40$ ) when no lubrication corrections are applied. Furthermore, the CCLM gives better results than the for the model H as soon as  $h = 1/40$ , even before any lubrication corrections (for the model H: Pearson's correlation coefficient equals to 0.9423,  $L^2|_{modelH}^{exp} = 0.0220 \text{ m.s}^{-1}$ ,  $L^\infty|_{modelH}^{exp} = 0.0891 \text{ m.s}^{-1}$ ).

Velocity				
$h$	$L^2 _h^{1/100}$	$L^\infty _h^{1/100}$	order $L^2$	order $L^\infty$
1/20	$2.13.10^{-4}$	$4.74.10^{-4}$		
1/40	$3.83.10^{-4}$	$6.35.10^{-4}$	–	–
1/60	$3.27.10^{-4}$	$5.48.10^{-4}$	2.04	1.95
1/80	$2.50.10^{-4}$	$3.75.10^{-4}$	1.73	1.58
Position				
$h$	$L^2 _h^{1/100}$	$L^\infty _h^{1/100}$	order $L^2$	order $L^\infty$
1/20	$2.07.10^{-3}$	$2.08.10^{-3}$		
1/40	$7.95.10^{-4}$	$8.24.10^{-4}$	1.81	1.81
1/60	$3.64.10^{-4}$	$3.90.10^{-4}$	1.62	1.62
1/80	$1.44.10^{-4}$	$1.64.10^{-4}$	1.54	1.53

Table 2: Table of convergence for the particle position and velocity, when the particle dynamic is fully resolved. The particle dynamic for  $h = 1/20$  is only fully resolved for large  $\epsilon$ , where the lubrication forces are not dominant. Therefore, errors on the particle position and velocity are unexpectedly small for  $h = 1/20$  compared to smaller  $h$ .

Using the same configuration described table 1, simulations have been performed with four different background grid resolutions  $h = 1/20$ ,  $h = 1/40$ ,  $h = 1/80$  and  $h = 1/100$ . The total hydrodynamic forces obtained are compared to the model H (Figure 11).

Far from the wall ( $\epsilon > 0.1$ ) higher grid resolution improves the capture of the total hydrodynamic forces. Indeed as shown on the figure 11, the hydrodynamic forces tend to the hydrodynamic force of the model H which fits experimental velocities (figure 10). As the particle goes closer to the wall ( $\epsilon < 0.1$ ) simulated hydrodynamic forces are underestimated compared to the solution of the model H, even before any lubrication correction is applied (see  $h = 1/80$  and  $h = 1/100$ ). Lower hydrodynamic forces induce higher particle velocities (than model H velocities) close to the wall, which leads to stronger response of the LLCM with steeper hydrodynamic force than with the model H. The relevance of the model H as reference for  $\epsilon < 0.1$  can be discussed since velocities of the model H do not perfectly fit experimental measurements in this range of  $\epsilon$  (figure 10).

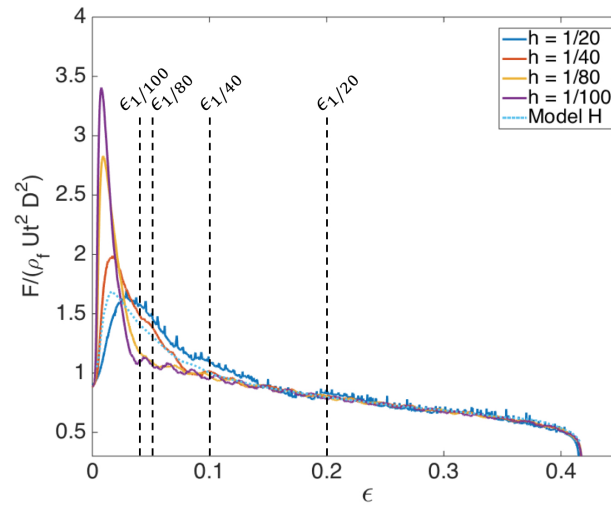


Figure 11: Total hydrodynamic force, according to the y-direction as a function of  $1/\epsilon$  during the approach phase. For each curve, lubrication correction is activated for  $\epsilon \leq \epsilon_h$ .

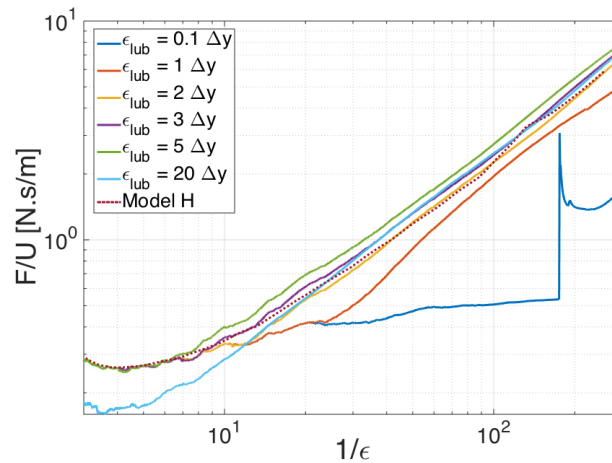


Figure 12: Total hydrodynamic force, according to the y-direction as a function of  $1/\epsilon$  during the approach phase for the critical lubrication distances  $\epsilon_{lub}$  equal to  $0.1\Delta x$ ,  $1\Delta x$ ,  $2\Delta x$ ,  $3\Delta x$ ,  $5\Delta x$ , and  $20\Delta x$ . Grid mesh resolution is  $h = 1/40$  for all curves.

The CCLM is a model with a single parameter  $\epsilon_{lub}$  which sets the minimum gap length where lubrication corrections are needed. Several simulations have been made for different  $\epsilon_{lub}$ . Figure 12 represents the total hydrodynamic force normalized by the particle velocity in respect to  $1/\epsilon$ .

Numerical simulations using  $\epsilon_{lub} \approx 2\Delta y$  are expected to give more realistic solutions since hydrodynamic forces better fit the model H solution. For smaller  $\epsilon_{lub}$ , hydrodynamic forces are underestimated leading to unrealistic mechanical contact and rebound of the particle (particle rebounds are not allowed by viscous effects for  $St < 10$ ). Simulations with high  $\epsilon_{lub}$  underestimate the total hydrodynamic force far from the wall, which decreases the solution accuracy.



The configuration of  $\epsilon_{lub}$  depends of the spacial discretization of the Navier Stokes equations, and needs to be adapted to the numerical method.

To complete our model reliability assessment, several simulations had been performed at higher Stokes numbers and compared to experimental data from Joseph *et al.*<sup>[41]</sup>. Figure 13 represents the distribution of the normalized effective coefficient of normal restitution of a particle according to the impact Stokes number. In order to be comparable to the measurements, we use the same technique and definition of the coefficient of normal restitution  $\xi_n$ , detailed by Joseph *et al.*<sup>[41]</sup>. By definition  $\xi_n = -U_R/U_T$  with  $U_R$  is the particle rebound velocity and  $U_T$  is the terminal velocity of the particle before the collision.

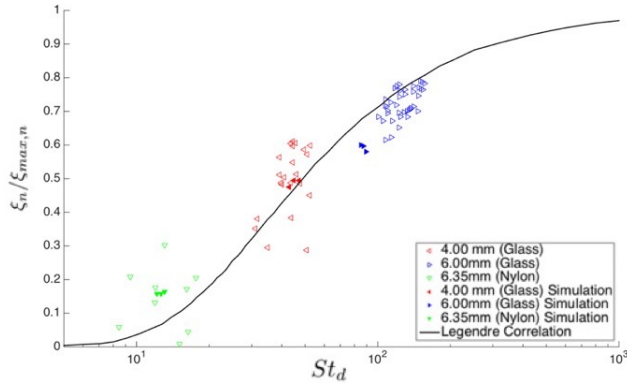


Figure 13: Distribution of normalized effective coefficient of normal restitution  $\xi_n/\xi_{max,n}$  of a single particle impacting a wall in respect of the particle Stokes number at the impact. Filled markers represent results obtained using LLCM using the same experimental setup than Joseph *et al.*<sup>[41]</sup> (data represented by hollow markers). The black curve represents a correlation made on experimental data proposed by Legendre *et al.*<sup>[42]</sup>

When the fluid does not influence the dynamic of the particle while colliding with an obstacle, the effective coefficient  $\xi_n$  is maximum and equal to the so called "dry coefficient of normal restitution"  $\xi_{max,n}$ . Experimental measurements reported in figure 13 show that "dry collision" occurs at high Stokes numbers where lubrication forces become negligible compared to the particle inertia. At low Stokes numbers  $St_d \lesssim 200$  lubrication forces are dominant. For  $St_d \sim 10$  lubrication effects prevent solid collision with the wall and maintain the particle in suspension above the wall.

Results with the local lubrication model (figure 13) are comparable to measurements and have a strong correlation with the experiment at a low Stokes number.

## 5.2 Oblique Impact of a Particle on a Wall

In order to validate the tangential component of the lubrication force, the oblique impact of a particle on a wall is the last case to validate our model. The same experimental setup than Joseph and Hunt<sup>[43]</sup> of oblique particle-wall collisions in the air and aqueous solutions has been used.

A single particle is immersed in a domain  $[19d, 5d, 3d]$  using a similar set-up than in section 5.1. The fluid is initially at rest and the particle is dropped without initial velocity as shown figure 14. In order to reproduce the experiment of Joseph and Hunt<sup>[43]</sup> the particle is linked to

$O$  by a virtual string of length  $L = 10$  cm. The tension of the string a virtual force  $\mathbf{F}_i^T$  collinear to  $\mathbf{e}_0 = \frac{\mathbf{X}_O - \mathbf{X}_i}{\|\mathbf{X}_O - \mathbf{X}_i\|}$  is added to the particle dynamic equation (28). The signed value of  $(\mathbf{F}_i^T \cdot \mathbf{e}_0)$  is found such that:

$$\mathbf{U}_i \cdot \mathbf{e}_0 = 0, \forall \|\mathbf{X}_O - \mathbf{X}_i\| \geq L + a, . \quad (46)$$

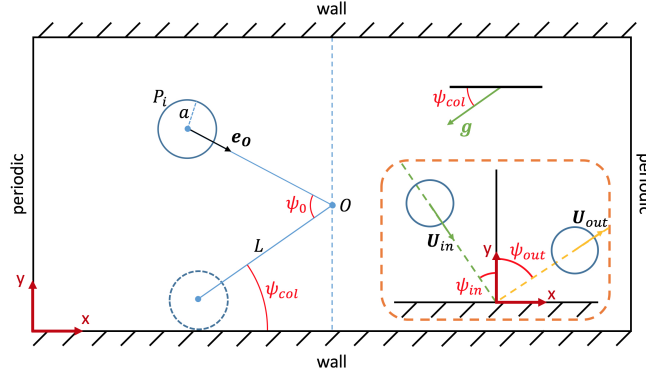


Figure 14: Sketch of the simulation domain and initial location of the particle. Inside the dashed box, particle characteristic velocities and angles are displayed before and after collision with the wall.

The pendulum is released from an angle  $\psi_0 = 18^\circ$  of its resting position  $\psi_{col}$  in contact with the wall (see figure 14) The gravity field  $\mathbf{g}$  is oriented such that  $\mathbf{g} = -g(\cos(\psi_{col})\mathbf{e}_x + \sin(\psi_{col})\mathbf{e}_y)$  and  $g = 9.81N.kg^{-1}$ .

Physical properties of the particle are presented in table 3 and have been chosen similar to Joseph and Hunt<sup>[43]</sup> experiments.

		Glass	Steel	
Particle density	$\rho_p$	2540	7780	$kg.m^{-3}$
Particle diameter	$d$	0.0127	0.0127	$m$
Normal restitution	$\xi_{max,n}$	0.97	0.97	
Tangent restitution	$\xi_{max,t}$	0.39	0.34	
Contact time	$t_c$	$1.10^{-7}$	$1.10^{-7}$	$s$
Friction coefficient	$\mu_c$	0.10	0.11	
Friction coefficient (wet)	$\mu_{c,wet}$	0.15	0.02	
Particle roughness	$a\epsilon_{col}$	$2.10^{-3}d$	$5.10^{-4}d$	$m$

Table 3: Particle properties.

Numerical simulations using CCLM have shown that the parameter  $n_{lub}$  has a limited impact on the results when  $n_{lub} > 10$ .

Figure 15 shows a comparison between the normalized incidence  $\Psi_{in} = \tan(\psi_{in})$  and rebound  $\Psi_{out} = \tan(\psi_{out})$  angles obtained from oblique collisions between steel and glass spheres in the air or water. In practice,  $\Psi_{in}$  and  $\Psi_{out}$  have been assessed using the following equations:

$$\begin{aligned} \Psi_{in} &= -\frac{\mathbf{V}_{C,in} \cdot \mathbf{e}_x}{\mathbf{V}_{C,in} \cdot \mathbf{e}_y}, \\ \Psi_{out} &= \frac{\mathbf{V}_{C,out} \cdot \mathbf{e}_x}{\mathbf{V}_{C,out} \cdot \mathbf{e}_y}, \end{aligned} \quad (47)$$

with  $\mathbf{V}_{C,in}$  and  $\mathbf{V}_{C,out}$  the velocities of the particle at the contact point just before and just after collision respectively. ( $\mathbf{V}_C = \mathbf{U}_i - a \boldsymbol{\Omega}_i \wedge \mathbf{e}_y$ ).

As highlighted by Joseph and Hunt<sup>[43]</sup>, piezoviscous effects in wet collision modify the coefficient of friction. Therefore, the modified (wet) friction coefficient (see table 3) is considered when the particle is immersed in water.

Numerical simulations have been performed with  $h = 1/40$  using 3200 particle mesh elements. Lubrication parameters have been chosen as  $\epsilon_{lub} = 2$  and  $n_{lub} = 100$ .

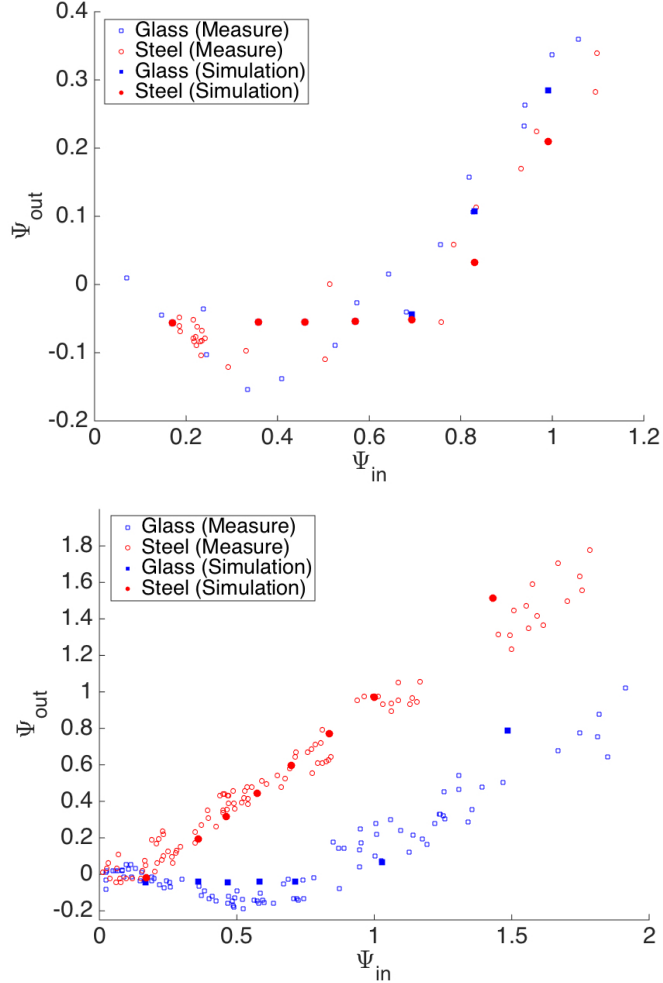


Figure 15: Comparison between the normalized incidence  $\Psi_{in}$  and rebound  $\Psi_{out}$  angles of steel (in red) and glass (in blue) particle in the air (on the top) or in aqueous solution (on the bottom) Results of simulations are represented by filled dots and are compared to Joseph and Hunt<sup>[43]</sup> experimental measurements (by circles).

Collisions of the particle immersed in the air are called dry collisions since the interactions between the solid particle and the surrounding fluid are neglectable. Simulations of dry collisions have been performed (figure 15, top) to check the collision model configurations and to assess the collision model accuracy with neglectable lubrication effects.

For wet collision (figure 15 bottom), hydrodynamic effects are no longer neglectable and the effect of the lubrication model can be assessed. The numerical simulations are in good agreement with the experimental data for the entire range of incidence angles.

## 6 Conclusion and Outlook

A local lubrication correction model for particle laden flow of spherical solid particles has been presented and validated. Interactions between a particle and an obstacle (another particle or a wall) can be decomposed into three types: long range hydrodynamics, short range hydrodynamics also called lubrication effects, and mechanical solid-solid contacts.

Long range hydrodynamic interaction are fully resolved by the Volume Penalization method (VP). The incompressible Navier-Stokes equations have been discretized in time using a scalar projection method and in space with a fully second order penalty method.

Due to unresolved scales associated with the grid, short range hydrodynamic interactions are, on the other hand, only partially captured by the numerical approach. We thus introduce a local lubrication model. This correction is based on asymptotic expansions of analytical solutions of particle-particle or particle-wall interactions, assuming that the flow within the gap between the particle and the obstacle is in the Stokes regime. Lubrication forces and torques are corrected in a neighborhood of the contact point of two interacting particles where lubrication is poorly captured, as long as the normalized gap width  $\epsilon$  is smaller than a critical length  $\epsilon_{lub}$  (a model parameter).

Finally, a linear soft-sphere collision model is used for solid-solid contacts. This model, widely used in the literature<sup>[31, 23]</sup>, represents mechanical contacts as two spring-dashpot systems connected at the contact point. The model allows stretching the collision time, to avoid computational overhead in the calculation of the collision force, making the method particularly efficient.

Our local lubrication correction model has been validated on several benchmarks. First, we considered a single particle falling onto a wall at various approach velocities. The comparison with experimental results<sup>[38, 41]</sup> enables us to validate the dominant lubrication component resulting from the squeezing of the fluid in the gap. The lubrication force and the torque created by the shearing of the fluid in the gap have been validated on oblique particle-wall collisions in dry and wet systems proposed by Joseph and Hunt<sup>[43]</sup>. The method will be generalized to non-spherical particle in future works.

## 7 Acknowledgements

The simulations presented in this paper were carried out using the PLAFRIM experimental parallel testbed, being developed under the Inria PlaFRIM development action with support from LABRI and IMB and other entities: Conseil Régional d'Aquitaine, FeDER, Université de Bordeaux and CNRS (see <https://plafirim.bordeaux.inria.fr/>).

## References

- [1] R. Sun and H. Xiao. CFD-DEM simulations of current-induced dune formation and morphological evolution. *Advances in Water Resources*, 92:228–239, 06/2016.

- 
- [2] J. Frohlich B. Vowinckel, T. Kempe and V. I. Nikora. *Numerical simulation of sediment transport in open channel flow*. Taylor & Francis Ltd, 2012.
- [3] J. F. Morris R. Mari, R. Seto and M. M. Denn. Shear thickening, frictionless and frictional rheologies in non-brownian suspensions. *Journal of Rheology*, 58(6):1693–1724, 2014.
- [4] A. Sierou and J. F. Brady. Accelerated stokesian dynamics simulations. *Journal of Fluid Mechanics*, 448:115–146, 12/2001.
- [5] E. Climent and M. R. Maxey. Numerical simulations of random suspensions at finite Reynolds numbers. *International Journal of Multiphase Flow*, 29(4):579–601, 04/2003.
- [6] M. R. Maxey and B. K. Patel. Localized force representations for particles sedimenting in stokes flow. *International Journal of Multiphase Flow*, 27(9):1603–1626, 09/2001.
- [7] D. D. Joseph H. H. Hu and M. J. Crochet. Direct simulation of fluid particle motions. *Theoretical and Computational Fluid Dynamics*, 3(5):285–306, 09/1992.
- [8] A. A. Johnson and T. E. Tezduyar. 3d simulation of fluid-particle interactions with the number of particles reaching 100. *Computer Methods in Applied Mechanics and Engineering*, 145(3-4):301–321, 05/1982.
- [9] M. Martin S. V. Apte and N. A. Patankar. A numerical method for fully resolved simulation (frs) of rigid particle-flow interactions in complex flows. *Inst. Chem. Eng. Symp.*, 228(8):2712–2738, 05/2009.
- [10] T. W. Pan R. Glowinski and J. Periaux. Distributed lagrange multiplier methods for incompressible viscous flow around moving rigid bodies. *Computer Methods in Applied Mechanics and Engineering*, 151(1-2):181–194, 01/1998.
- [11] N. Sharma and N. A. Patankar. A fast computation technique for the direct numerical simulation of rigid particulate flows. *Journal of Computational Physics*, 205(2):439–457, 05/2005.
- [12] J. A. Simeonov and J. Calantoni. Modeling mechanical contact and lubrication in direct numerical simulations of colliding particles. *International Journal of Multiphase Flow*, 46:38–53, 2014.
- [13] A. Wachs. A DEM-DLM/FD method for direct numerical simulation of particulate flows: Sedimentation of polygonal isometric particles in a newtonian fluid with collisions. *Computers & Fluids*, 38(8):1608–1628, 09/2009.
- [14] X. Shao Z. Yu and A. Wachs. A fictitious domain method for particulate flows with heat transfer. *Journal of Computational Physics*, 217(2):424–452, 09/2006.
- [15] B. Merlet A. Lefebvre-Lepot and T. N. Nguyen. An accurate method to include lubrication forces in numerical simulations of dense stokesian suspensions. *Journal of Fluid Mechanics*, 769:369–386, 2015.
- [16] A. J. C. Ladd and R. Verberg. Lattice-Boltzmann simulations of particle-fluid suspensions. *Journal of Statistical Physics*, 140(5):1191–1251, 09/2001.
- [17] Z. G. Feng and E. E. Michaelides. Proteus: a direct forcing method in the simulations of particulate flow. *Journal of Computational Physics*, 202(1):20–51, 01/2005.

- [18] M. Uhlmann. An immersed boundary method with direct forcing for the simulation of particulate flows. *Journal of Computational Physics*, 209(2):448–476, 11/2005.
- [19] P. Angot, C.-H. Bruneau, and P. Fabrie. A penalization method to take into account obstacles in incompressible flows. *Numer. Math.*, 81(4):497–520, 1999.
- [20] F. Radjai and F. Dubois. *Discrete-element Modeling of Granular Materials*. Wiley, 03/2011.
- [21] M. D. A. Cooley and M. E. O’Neill. On the slow motion generated in a viscous fluid by the approach of a sphere to a plane wall or stationary sphere. *Mathematika*, 16(1):37–49, 1969.
- [22] O’Neill M. E. and K. Stewartson. On the slow motion of a sphere parallel to a nearby plane wall. *Journal of Fluid Mechanics*, 27(4):705–724, 03/1967.
- [23] T. Bonometti E. Iazard and L. Lacaze. Modelling the dynamics of a sphere approaching and bouncing on a wall in a viscous fluid. *Journal of Fluid Mechanics*, 747:422–446, 2014.
- [24] L. Lobry S. Gallier, E. Lemaire and F. Peters. A fictitious domain approach for the simulation of dense suspensions. *Journal of Computational Physics*, 256:367–387, 01/2014.
- [25] J. Wells Y. Nguyen and H. Truong. A fictitious-domain simulation of solid-liquid flow with subgrid lubrication force correction; a sphere falling onto a plane surface. *Proceedings of Hydraulic Engineering*, 51:151–156, 2007.
- [26] O. R. Walton. *Numerical simulation of inelastic, frictional particle-particle interactions*. Butterworth-Heinemann, 1993.
- [27] S. Kim and S. Karrila. *Microhydrodynamics: Principles and Selected Applications*. Dover Publications Inc., 1991.
- [28] D. J. Jeffrey. Low Reynolds number flow between converging spheres. *Mathematika*, 29(1):58–66, 05/1982.
- [29] M. Stimson and G. B. Jeffery. The motion of two spheres in a viscous fluid. *The Royal Society*, 111(757), 05/1926.
- [30] J. Happel and H. Brenner. *Low Reynolds Number Hydrodynamics*. M. Nijhoff, 1983.
- [31] J. Westerweel P. Costa, B. J. Boersma and W. P. Breugem. Collision model for fully-resolved simulations of flows laden with finite-size particles. *Physical Review E*, 92(5), 10/2015.
- [32] M. Bergmann and A. Iollo. Bioinspired swimming simulation. *Journal of Computational Physics*, 323C:310–321, 2016.
- [33] A.J. Chorin. Numerical solution of the Navier-Stokes equations. *Math. Comp.*, 22:745–762, 1968.
- [34] R. Temam. Sur l’approximation de la solution des équations de Navier-Stokes par la méthode des pas fractionnaires II. *Archiv. Rat. Mech. Anal.*, 32:377–385, 1969.
- [35] M. Bozkurtas F. M. Najjar A. Vargas R. Mittal, H. Dong and A. von Loebbecke. A versatile sharp interface immersed boundary method for incompressible flows with complex boundaries. *Journal of Computational Physics*, 227(10):4825–4852, 05/2008.

- 
- [36] Y. Saad and M. H. Schultz. GMRES: A generalized minimal residual algorithm for solving nonsymmetric linear systems. *Society for Industrial and Applied Mathematics*, 7(3):856–869, 07/1986.
- [37] J. Hovnanian M. Bergmann and A. Iollo. An accurate cartesian method for incompressible flows with moving boundaries. *Communications in Computational Physics*, 15(5):1266–1290, 05/2014.
- [38] T. Tanaka S. Harada and Y. Tsuji Tsuji. Fluid force acting on a particle falling toward a wall. *JSME International Journal Series B*, 44(4):520–525, 11/2001.
- [39] M. J. Adams and V. Perchard. The cohesive forces between particles with interstitial liquid. *Inst. Chem. Eng. Symp.*, 91:147–156, 1985.
- [40] S. L. Soo. *Fluid Dynamics of Multiphase Systems*. Blaisdell Publishing Company, 1967.
- [41] M. L. Hunt G. G. Joseph, R. Zenit and A. M. Rosenwinkel. Particle-wall collisions in a viscous fluid. *Journal of Fluid Mechanics*, 433:329–346, 04/2001.
- [42] C. Daniel D. Legendre and P. Guiraud. Experimental study of a drop bouncing on a wall in a liquid. *Physics of Fluids*, 17(9), 09/2005.
- [43] G. G. Joseph and M. L. Hunt. Oblique particle-wall collisions in a liquid. *Journal of Fluid Mechanics*, 510:71–93, 2004.



**RESEARCH CENTRE  
BORDEAUX – SUD-OUEST**

200 avenue de la Vieille Tour  
33405 Talence Cedex

Publisher  
Inria  
Domaine de Voluceau - Rocquencourt  
BP 105 - 78153 Le Chesnay Cedex  
[inria.fr](http://inria.fr)

ISSN 0249-6399